Chemical Science

EDGE ARTICLE

View Article Online
View Journal | View Issue

Cite this: *Chem. Sci.*, 2017, **8**, 2581

# The tetrahedral structure and luminescence properties of Bi-metallic $Pt_1Ag_{28}(SR)_{18}(PPh_3)_4$ nanocluster†

Xi Kang,[a] Meng Zhou,[b] Shuxin Wang,[a] Shan Jin,[a] Guodong Sun,[a] Manzhou Zhu*[a] and Rongchao Jin*[b]

Received 19th November 2016
Accepted 4th January 2017

DOI: 10.1039/c6sc05104a

www.rsc.org/chemicalscience

The atomic-structure characterization of alloy nanoclusters (NCs) remains challenging but is crucial in order to understand the synergism and develop new applications based upon the distinct properties of alloy NCs. Herein, we report the synthesis and X-ray crystal structure of the $Pt_1Ag_{28}$(S-Adm)$_{18}$($PPh_3$)$_4$ nanocluster with a tetrahedral shape. $Pt_1Ag_{28}$ was synthesized by reacting $Pt_1Ag_{24}(SPhMe_2)_{18}$ simultaneously with Adm-SH (1-adamantanethiol) and $PPh_3$ ligands. A tetrahedral structure is found in the metal framework of $Pt_1Ag_{28}$ NC and an overall surface shell ($Ag_{16}S_{18}P_4$), as well as discrete $Ag_4S_6P_1$ motifs. The $Pt_1Ag_{12}$ kernel adopts a face-centered cubic (FCC) arrangement, which is observed for the first time in alloy nanoclusters in contrast to the commonly observed icosahedral structure of homogold and homosilver NCs. The $Pt_1Ag_{28}$ nanocluster exhibits largely enhanced photoluminescence (quantum yield QY = 4.9%, emission centered at ~672 nm), whereas the starting material ($Pt_1Ag_{24}$ NC) is only weakly luminescent (QY = 0.1%). Insights into the nearly 50-fold enhancement of luminescence were obtained *via* the analysis of electronic dynamics. This study demonstrates the atomic-level tailoring of the alloy nanocluster properties by controlling the structure.

## 1 Introduction

Atomically precise metal nanoclusters (NCs) have attracted increasing interest as functional materials due to their distinct optical, catalytic, magnetic, and electrochemical properties.[1–7] The well-defined structure of NCs with precise compositions permits atomic level structure–property correlations.[8–18] To date, great progress has been achieved in the synthesis and characterization of NCs, including mono-metallic NCs (gold or silver) and alloy NCs.[19–26] Among them, bi-metallic NCs may offer significantly enhanced properties compared to that of the single-component NCs due to the synergistic effects induced by the heteroatom(s).[20b,21b,22b,23,25a] For example, drastically improved catalytic activity and enhanced luminescence (compared with the mono-metallic counterparts of NCs) have been achieved in M–Au (with a single dopant M = Pt or Pd)[27,28] and Au–Ag bi-metallic NCs (with Au dopants),[21b,22b] respectively. These results demonstrate the great potential of alloy NCs in catalytic, optical and biological applications.

Thus far, the atomic-level structural determination of bi-metallic NCs by X-ray crystallography has only been achieved in a few cases.[11,20a,21b,22–26] The synthetic methods used to prepare bimetallic NCs can be roughly classified into two strategies: (1) the co-reduction of two metal precursors (*e.g.* complexes) in one-pot reactions[7,11,20,21b,22b,24] and (2) doping mono-metallic NCs (which serve as templates) with heteroatom complexes.[25a,29–32] For the synthesis of mono-metallic NCs, the thiol etching-induced transformation method is commonly used,[19,33] which gives rise to NCs with novel structures and distinct properties. However, this etching strategy has not been applied to the synthesis of alloy NCs. The etching strategy is highly attractive for alloy NCs because the heteroatom(s) can be regarded as labelling atom(s), which provide mechanistic insights into the etching process (similar to the isotope tracing method used in molecular chemistry).

Herein, we report the attainment of $Pt_1Ag_{28}$ nanocluster co-protected by 1-adamantanethiolate (HS-Adm) and triphenyl phosphine ($PPh_3$) ligands, formulated as $Pt_1Ag_{28}$(S-Adm)$_{18}$($PPh_3$)$_4$. The $Pt_1Ag_{28}$ nanoclusters are obtained by etching $Pt_1Ag_{24}(SPhMe_2)_{18}$ with both the HS-Adm and $PPh_3$ ligands, and the crystal structure of $Pt_1Ag_{28}$ reveals that the Pt atom resides in the central position of the nanocluster. In addition, $Pt_1Ag_{28}$ shows unique structural features including: (1) the presence of a face-centered cubic (FCC) $Pt_1Ag_{12}$ kernel, which is observed for the first time in silver-based alloy NCs, as opposed to the common icosahedral structure, and (2) the discovery of new

[a]Department of Chemistry and Center for Atomic Engineering of Advanced Materials, Anhui University, Hefei, Anhui 230601, China. E-mail: zmz@ahu.edu.cn

[b]Department of Chemistry, Carnegie Mellon University, Pittsburgh, PA 15213, USA. E-mail: rongchao@andrew.cmu.edu

† Electronic supplementary information (ESI) available. CCDC 1495551. For ESI and crystallographic data in CIF or other electronic format see DOI: 10.1039/c6sc05104a

surface motifs, such as the $Ag_4(SR)_6(PPh_3)_1$ motif and its assembled cage-like structure that protects the FCC kernel. Furthermore, compared to the $Pt_1Ag_{24}$ precursor, the photoluminescence (PL) quantum yield (QY) of $Pt_1Ag_{28}$ is largely increased from 0.1% to 4.9% (*i.e.* about 50 times of enhancement) due to the suppressed relaxation of the excited state *via* phonon emission and other non-radiative pathways. Moreover, a significant enhancement in the thermal stability was also achieved in $Pt_1Ag_{28}$ compared to that of the $Pt_1Ag_{24}$ precursor nanocluster.

## 2 Experimental

### Materials

Hexachloroplatinic(IV) acid ($H_2PtCl_6\cdot6H_2O$, 99.99%, metals basis), silver nitrate ($AgNO_3$, 99%, metals basis), 2,4-dimethylbenzenethiol ($HSPhMe_2$, 99%), 1-adamantanethiol ($C_{10}H_{16}S$, 99%), triphenylphosphine ($PPh_3$, 99%), tetraphenyl phosphonium bromide ($PPh_4Br$, 98%) and sodium borohydride ($NaBH_4$, 99.9%). Methylene chloride ($CH_2Cl_2$, HPLC grade, Aldrich), ethyl acetate ($CH_3COOC_2H_5$, HPLC, Aldrich), methanol ($CH_3OH$, HPLC, Aldrich) and *n*-hexane (Hex, HPLC grade, Aldrich). Pure water was purchased from Wahaha Co. Ltd. All reagents were used as received without further purification. All glassware were thoroughly cleaned with aqua regia ($HCl:HNO_3$ = 3 : 1 vol%), rinsed with copious amounts of pure water and then dried in an oven prior to use.

### Synthesis of the $[Pt_1Ag_{24}(SPhMe_2)_{18}](PPh_4)_2$ nanocluster

For the nanocluster synthesis, $AgNO_3$ (30 mg, 0.18 mmol) was dissolved in 5 mL of $CH_3OH$ and 15 mL of $CH_3COOC_2H_5$. $H_2PtCl_6\cdot6H_2O$ (4 mg, 0.0075 mmol) was dissolved in 5 mL of $CH_3OH$ and added to the reaction mixture. The resulting solution was vigorously stirred (about 1200 rpm) with a magnetic stirrer bar for 15 min. Then, 100 μL of $HSPhMe_2$ was added. After another 15 min, 1 mL of $NaBH_4$ aqueous solution (20 mg $mL^{-1}$) was added quickly to the reaction mixture under vigorous stirring. The reaction was allowed to proceed for 24 hours under a $N_2$ atmosphere. After the reaction was complete, the mixture in the organic phase was rotavaporated under vacuum, and then 20 mL of $CH_3OH$ was used to extract the product, which also contained the redundant $HSPhMe_2$ and by-products. 5 mL of a $CH_3OH$ solution containing excess $PPh_4Br$ was added into the abovementioned $CH_3OH$ solution. Subsequently, the resulting solution was centrifuged to obtain the solid. Approximately 15 mL of methanol was added to wash the synthesized nanocluster. The precipitate was then dissolved in $CH_2Cl_2$ giving rise to $[Pt_1Ag_{24}(SPhMe_2)_{18}](PPh_4)_2$ nanoclusters (34 mg, 0.006 mmol, yield: 80.5% on a Ag mole basis).

### Synthesis of $Pt_1Ag_{28}(S\text{-}Adm)_{18}(PPh_3)_4$ nanocluster

For the nanocluster synthesis, 10 mg of $(PPh_4)_2[Pt_1Ag_{24}(SPhMe_2)_{18}]$ was dissolved in 10 mL of $CH_2Cl_2$. Then, 5 mg of $PPh_3$ and 10 mg of AdmSH were added to the solution simultaneously. The reaction was allowed to proceed for 30 min at room temperature. The colour of solvent transformed from bright green to orange. The organic layer was separated from the precipitate and evaporated to dryness. The $Pt_1Ag_{28}(S\text{-}Adm)_{18}(PPh_3)_4$ nanocluster was obtained afterwards. The dried nanocluster was washed with methanol at least 3 times and collected by centrifugation (7 mg, 0.001 mmol, yield: 63.2% on a Ag mole basis).

### Characterization

All UV-vis absorption spectra of the nanoclusters dissolved in $CH_2Cl_2$ were recorded using an Agilent 8453 diode array spectrometer, whose background correction was made using a $CH_2Cl_2$ blank. Solid samples were dissolved in $CH_2Cl_2$ to make a dilute solution with its subsequent transformation to a 1 cm path length quartz cuvette, which was followed by the spectral measurements. Thermogravimetric analysis (TGA) was carried out on a thermogravimetric analyzer (DTG-60H, Shimadzu Instruments, Inc.) with 5 mg of nanocluster in a $SiO_2$ pan at a heating rate of 10 K $min^{-1}$ from room temperature (about 298 K) to 1073 K. X-ray photoelectron spectroscopy (XPS) measurements were performed on a Thermo ESCALAB 250, configured with a monochromated Al Kα (1486.8 eV) 150 W X-ray source, 0.5 mm circular spot size, a flood gun to counter charging effects, and a analysis chamber base pressure lower than $1 \times 10^{-9}$ mbar; data were collected at FAT = 20 eV. Photoluminescence spectra were measured on a FL-4500 spectrofluorometer with the same optical density (OD) ~0.05. In these experiments, the nanocluster solutions were prepared in $CH_2Cl_2$ at a concentration of less than 1 mg $mL^{-1}$. Absolute quantum yields (QY) were measured using dilute solutions of the clusters (0.05 OD absorption at 480 nm) on a HORIBA FluoroMax-4P. Inductively coupled plasma-atomic emission spectrometry (ICP-AES) measurements were performed on an Atomscan Advantage instrument made by Thormo Jarrell Ash Corporation (USA). The nanoclusters were digested with concentrated nitric acid and the concentration of the nanoclusters was set to ~0.5 mg $L^{-1}$.

### Single-crystal growth and analysis

Single crystals of the $Pt_1Ag_{28}(S\text{-}Adm)_{18}(PPh_3)_4$ nanocluster were grown at 4 °C for 2–3 days in $CH_2Cl_2$/hexane. Red crystals were collected and the structures of $Pt_1Ag_{28}(S\text{-}Adm)_{18}(PPh_3)_4$ were determined. The data collection for single crystal X-ray diffraction was carried out on a Bruker Smart APEX II CCD diffractometer under a liquid nitrogen flow at 150 K using graphite-monochromatized Cu Kα radiation ($\lambda$ = 1.54178 Å). Data reductions and absorption corrections were performed using the SAINT and SADABS programs, respectively. The structure was solved using direct methods and refined with full-matrix least squares on $F^2$ using the SHELXTL software package. All non-hydrogen atoms were refined anisotropically, and all the hydrogen atoms were set in geometrically calculated positions and refined isotropically using the riding model.

### Femto-nanosecond transient absorption spectra

Details of the femtosecond experiments have been described elsewhere.[37] Nanosecond transient absorption spectra were measured based on the same ultrafast pump pulses along with an electronically delayed supercontinuum light source with a sub-nanosecond pulse duration (EOS, Ultrafast Systems).

**Time-correlated single-photon counting**

Fluorescence lifetimes were measured using a time-correlated single photon counting (TCSPC) technique (Fluorolog-3 HORIBA Jobin Yvon); a pulsed LED source (376 nm, 1.1 ns) was used as the excitation source. The instrument response function (IRF) of detection was about 1.5 ns.

## 3 Results and discussion

**Characterization of the reaction**

The reaction was monitored *via* UV-vis spectroscopy (Fig. 1A), in which the spectra show the gradual conversion of $Pt_1Ag_{24}(SR)_{18}$ to $Pt_1Ag_{28}(S\text{-}Adm)_{18}(PPh_3)_4$ when reacting with Adm-SH and $PPh_3$ together as reflected in the spectral changes. For a close comparison, the spectra of $Pt_1Ag_{24}$ and the etching product $Pt_1Ag_{28}$ are shown in Fig. 1B, in which one can see that the 465 and 600 nm absorption bands of $Pt_1Ag_{24}$ are blue-shifted to 445 and 545 nm, respectively, after the conversion. In addition, we tested Adm-SH as the sole etching reagent in this reaction. The product was a mixture of larger nanoclusters as opposed to pure $Pt_1Ag_{28}$ (Fig. S2†).

Thermogravimetric analysis (TGA) of the product shows a total weight loss of 56.8 wt% (Fig. 1C), which is consistent with the theoretical loss (55.8 wt%) according to the formula determined *via* X-ray crystallography (*vide infra*); it should be noted that the loss of $PPh_3$ ligands accounts for 15.2 wt% and S-Adm ligands for 41.6 wt% (Fig. 1C), which is also consistent with the theoretical losses (14.4 and 41.4 wt%, respectively). The atomic ratio of Pt to Ag was analyzed *via* inductively coupled plasma (ICP) atomic emission spectroscopy to be Pt/Ag = 3.9/96.1 and also by X-ray photoelectron spectroscopy (XPS) to be Pt/Ag = 3.5/96.5, which are consistent with the expected ratio of Pt/Ag = 3.5/96.5 (see Fig. 1D, S3 and Table S1† for the data and details). Electrospray ionization mass spectrometry (ESI-MS) confirmed the purity of $Pt_1Ag_{28}$ (Fig. S4†), in the results of which only one peak was found ($m/z$ = 3637.67 Da, with $z$ = 2+ and perfectly matched the experimental and simulated isotope patterns of $[Pt_1Ag_{28}(SR)_{18}(PPh_3)_4]^{2+}$).

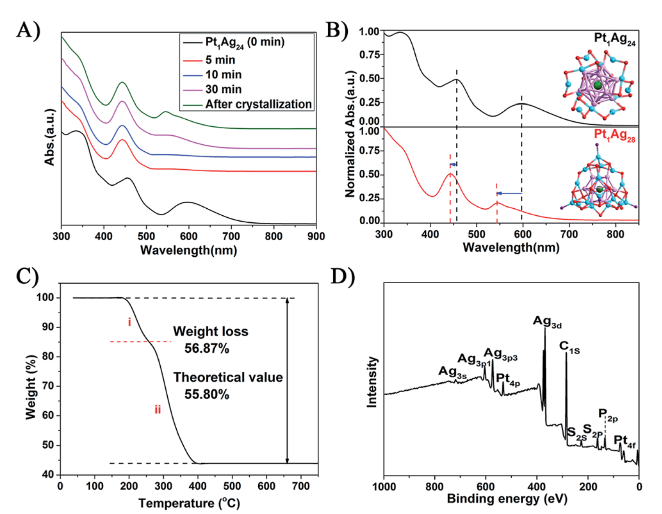


Fig. 1 (A) The evolution of the etching of $Pt_1Ag_{24}(SR)_{18}$ with co-present AdmSH and $PPh_3$ ligands. (B) The UV-vis spectral comparison of the $Pt_1Ag_{24}$ and $Pt_1Ag_{28}$ NCs. Insets: the X-ray crystal structures of $Pt_1Ag_{24}$ and $Pt_1Ag_{28}$. Color codes: green spheres = Pt; cerulean sphere = Ag on the shell; violet sphere = Ag in the kernel; red sphere = S; purple sphere = P; carbon tails are omitted for clarity. (C) TGA of $Pt_1Ag_{28}$. (D) XPS spectrum of $Pt_1Ag_{28}$.

**Atomic structure**

The structure of $Pt_1Ag_{28}$ can be divided into two parts, the kernel and the surface shell. By comparing the crystal structures of the $Pt_1Ag_{24}$ and $Pt_1Ag_{28}$ nanoclusters, we identified that the six $Ag_2S_3$ (–R groups omitted) staple motifs surrounding the $Pt_1Ag_{12}$ kernel in the $Pt_1Ag_{24}$ nanocluster change to the four $Ag_4S_6P_1$ motifs sharing six S atoms, forming an overall $Ag_{16}S_{18}P_4$ shell in a tetrahedral shape with the 4 motifs at the 4 vertices of tetrahedron (Fig. 2). As for the kernel structure, the icosahedral $Pt_1Ag_{12}$ kernel of $Pt_1Ag_{24}$ was converted into an FCC kernel (*vide infra*). The single Pt atom is surrounded by an $Ag_{12}$ shell to form the $Pt_1Ag_{12}$ kernel. The $Pt_1Ag_{12}$ kernel was further encircled by an integrated $Ag_{16}S_{18}P_4$ cage-like exterior shell. Thus, the entire structure shows a tri-stratified arrangement—Pt(center)@$Ag_{12}$(shell)@$Ag_{16}S_{18}P_4$ (exterior). The bond lengths and bond angles are given in the ESI (Table S2†).

For a better view, the overall $Ag_{16}S_{18}P_4$ shell was dissected into four equivalent $Ag_4S_6P_1$ motifs sharing six S atoms. The six S atoms in each $Ag_4S_6P_1$ motif are divided into two forms (Fig. 2A and B): (1) the three S atoms (in red, vertically linking to the Ag atoms) bond to the Ag atoms in the kernel–shell (3 × 4 = 12Ag atoms in the $M_{13}$ kernel), which can be regarded as the bridges between the kernel and motif outside. The total 12S atoms stabilize the $M_{13}$ kernel in the overall structure; (2) the other three S atoms (in orange, connecting the bottom Ag atoms) act as linkers to connect two nearby $Ag_4S_6P_1$ motifs to

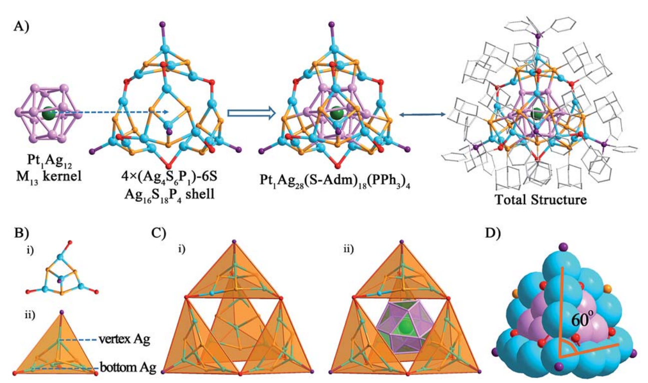


Fig. 2 Ball-and-stick views of (A) the $Pt_1Ag_{12}$ kernel, outer-motif and the overall structure; (B) the $Ag_4S_6P_1$ motif in the tetrahedral shape and (C) the total structure in the tetrahedral shape. (D) A space-filling view of the nanocluster. Color codes: green spheres, Pt; cerulean sphere, Ag on the shell; violet sphere, Ag in the kernel; orange sphere, S bonding the kernel; red sphere, S linking the motifs; purple sphere, P. For clarity, the hydrogen atoms are not shown.

form the integrated motif shell—$Ag_{16}S_{18}P_4$. Interestingly, the P atom and three bottom S atoms in each $Ag_4S_6P_1$ motif constitute a tetrahedral structure. The overall $Ag_{16}S_{18}P_4$ shell consists of four $Ag_4S_6P_1$ tetrahedral motifs (Fig. 2C), and the integrated configuration is also approximately a tetrahedron. The overall metal framework of $Pt_1Ag_{28}$ (Fig. 2D) also adopts a tetrahedral shape, which is constructed by six 4-atom-long edges (Ag atoms from the shell) and four faces of $Ag_3$ (Ag atoms from the kernel). In addition, the angle between the edges is approximately 60° (Fig. 2D), which is consistent with the standard tetrahedral structure.

As to the structure of the $Pt_1Ag_{12}$ kernel, the icosahedral kernel of $Pt_1Ag_{24}$ was transformed to the FCC arrangement in $Pt_1Ag_{28}$ after the etching process. To the best of our knowledge, all the previously reported $M_{13}$ (M = Au/Ag/Pt) kernels are icosahedral, and thus the FCC arrangement in the $M_{13}$ kernel was observed for the first time in an alloy NC. Based on the well-defined structure of $Pt_1Ag_{24}$ and $Pt_1Ag_{28}$, we propose a plausible mechanism for the transformation process. As shown in Fig. 3, the $Pt_1Ag_{12}$ kernel of $Pt_1Ag_{24}$ is in an icosahedral arrangement by the triangular shape of each face. When etched with Adm-SH and $PPh_3$ ligands, the relative positions of the Ag atoms on the kernel's surface shift, and consequently the bonds of the $Pt_1Ag_{12}$ kernel in $Pt_1Ag_{24}$ (*i.e.* bonds i–iii in Fig. 3A, 2.960–2.991 Å) stretch to ~3.610 Å, indicating that the Ag–Ag bonds were broken. Simultaneously, the angle $\alpha$ enlarges from 73.6° to 84.7°. Thus, some of the triangular faces in the kernel of $Pt_1Ag_{24}$ are rearranged into a quadrilateral in $Pt_1Ag_{28}$ and the kernel is thus converted from an icosahedral to FCC arrangement. Furthermore, the slight distortion of the $Pt_1Ag_{12}$ kernel in $Pt_1Ag_{28}$ compared to the typical FCC $M_{13}$ kernel (Fig. 3C) was caused by the interaction between the kernel and the outside motifs.

As mentioned earlier, the heteroatom(s) can be used as labeling atom(s) to shed light on the mechanism of the structural transformation. In this study, the central position of the Pt atom (as the only heteroatom) was retained during the etching process. This phenomenon indicates that the $M_{13}$ kernel of $Pt_1Ag_{24}$ does not fall apart in the etching process and instead it just becomes distorted in response to the transformation of the exterior motifs. On the other hand, the stability of the central Pt atom was also established in the $Pt_1Ag_{24}$ and $Pt_1Au_{24}$ cases using density functional theory (DFT) calculations and experimental studies.[20b,28]

Recently, an $Ag_{29}$ NC co-protected with BDT (1,3-benzenedithiol) and $PPh_3$ ligands as well as a single Au doped $Au_1Ag_{28}$

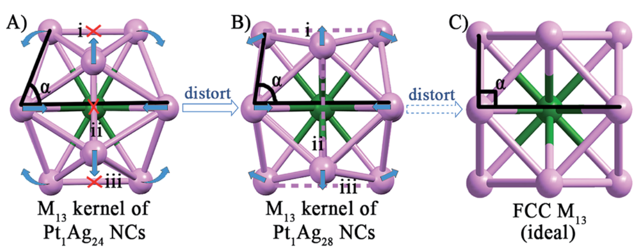


Fig. 3 The $Pt_1Ag_{12}$ kernels of the (A) $Pt_1Ag_{24}$ and (B) $Pt_1Ag_{28}$ NCs. (C) The standard FCC $M_{13}$ kernel. Color codes: green sphere, Pt; violet sphere, Ag.

NC have been reported by Bakr and co-workers.[22] In the present study, we discovered that the framework of $Pt_1Ag_{28}$ was largely different from $Ag_{29}$ and $Au_1Ag_{28}$, albeit all of them have the same metal atom number (*i.e.* 29). The distinct differences in $Pt_1Ag_{28}$ compared to the other two examples are manifested in the following (see Fig. S5–8†): (1) the kernels of $Ag_{29}$ and its Au-doped alloy are an icosahedral $M_{13}$, whereas $Pt_1Ag_{28}$ possesses an FCC $Pt_1Ag_{12}$ kernel; (2) the motifs on the nanocluster surface are also entirely different; the $Ag_{29}$ (or $Au_1Ag_{28}$) NC possesses four $Ag_1S_3P_1$ and four $Ag_3S_3$ motifs (carbon tails omitted), whereas the $Pt_1Ag_{28}$ is comprised of four new $Ag_4S_6P_1$ motifs. By sharing six thiolates, the four $Ag_4S_6P_1$ motifs form a cage-like $Ag_{16}S_{18}P_4$ structure; (3) in the $Pt_1Ag_{28}$ nanocluster, all the metal atoms are located within the tetrahedron constructed *via* the four P atoms, while in $Ag_{29}$ and $Au_1Ag_{28}$, 12Ag atoms out of the 29 metal atoms overflow the corresponding tetrahedron (*i.e.*, only 17 atoms are completely contained in the tetrahedron). In addition, it should be noted that tetrahedron-shaped Au NCs have been studied previously[34] and our study fills in the blank in tetrahedral Ag NCs; (4) several smaller tetrahedral units were found in $Pt_1Ag_{28}$, such as the $Ag_4S_6P_1$ motifs, the assembled motif structure and the overall metal nanocluster structure; however, such tetrahedrons are not observed in the $Ag_{29}$ and $Au_1Ag_{28}$ NCs; (5) a charge state of −3 was reported for $Ag_{29}$ and $Au_1Ag_{28}$ with an electron count of 8e (that is, $29 - 24 + 3 = 8e$). In $Pt_1Ag_{28}$, ESI-MS (Fig. S4†) identified that the cluster bears 2+ charges (not 3− in $Ag_{29}$ and $Au_1Ag_{28}$), but the X-ray crystallographic analysis did not find any counter ion (presumably $Cl^-$ disordered in the crystal). Taking the results together, the nominal electron count of $Pt_1Ag_{28}$ is 8e (that is, $28 - 18 - 2 = 8e$).

**The optical energy gaps and photoluminescence properties.** To further compare the properties of the $Pt_1Ag_{28}$ with $Pt_1Ag_{24}$, the absorption spectra and PL of both samples were analyzed. The energy-scale absorption spectra of $Pt_1Ag_{24}$ and $Pt_1Ag_{28}$ are shown in Fig. 4A, with the optical energy gap of $Pt_1Ag_{24}$ being 1.72 eV and $Pt_1Ag_{28}$ being 1.86 eV. To the naked eye, the solution color of $Pt_1Ag_{24}$ is green, whereas the solution color of $Pt_1Ag_{28}$ is orange (insets of Fig. 4A). The trend of the optical gap energies was a surprise since typically one would expect the larger size of $Pt_1Ag_{28}$ to have a smaller gap than that of $Pt_1Ag_{24}$.

With respect to the PL properties (Fig. 4B), the QY of $Pt_1Ag_{24}$ is very low (0.1%),[20b] but interestingly the QY is largely increased to 4.9% in $Pt_1Ag_{28}$ (by about a 50-fold enhancement). The PL of $Pt_1Ag_{28}$ is strong enough to be perceived by the naked eye. In addition, the PL peak of $Pt_1Ag_{24}$ was centered at 728 nm but it blue-shifts to 672 nm in $Pt_1Ag_{28}$ (a shift of *ca.* 56 nm). The PL excitation spectrum of $Pt_1Ag_{28}$ was also measured, which is almost identical to its absorption spectrum (Fig. S9†), indicating typical quantum confinement behavior and electron relaxation to the LUMO level before fluorescing.

**The excited state behavior of $Pt_1Ag_{24}$ and $Pt_1Ag_{28}$.** Femto-nanosecond transient absorption spectroscopy (fs–ns TA) and time-correlated single-photon counting (TCSPC) were performed on both the $Pt_1Ag_{24}$ and $Pt_1Ag_{28}$ nanoclusters in order to probe their excited state properties. Upon excitation at 360 nm, $Pt_1Ag_{24}$ exhibits net ground state bleaching (GSB) at 450 nm and 580 nm, which corresponds to the UV-vis absorption and

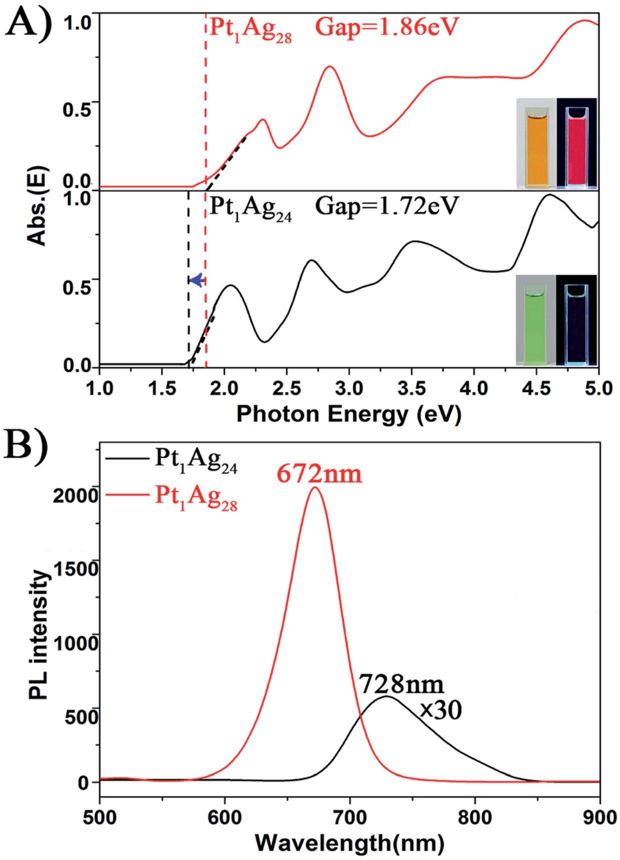


Fig. 4 The spectra on the (A) energy scale and (B) PL of the $Pt_1Ag_{24}$ and $Pt_1Ag_{28}$ NCs. Insets of (A): digital photographs of each nanocluster in $CH_2Cl_2$ solution under visible and UV light.

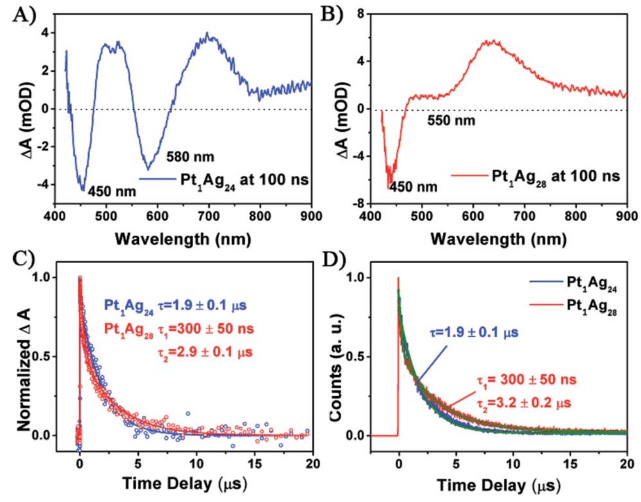


Fig. 5 The transient absorption spectra at a time delay = 100 ns for (A) $Pt_1Ag_{24}$ and (B) $Pt_1Ag_{28}$ with excitation at 360 nm. (C) Normalized kinetic traces obtained from the transient absorption of both nanoclusters. (D) Normalized kinetic traces of fluorescence decay of both clusters at the emission maxima measured using TCSPC. All the solid lines are fits of the data.

excited state absorption (ESA) around 500 nm and 700 nm (Fig. 5A). For $Pt_1Ag_{28}$ (Fig. 5B), the TA spectra exhibit an ESA centered at 650 nm, a net GSB around 450 nm and a dip around 550 nm, which also agrees with the steady state absorption. The kinetic traces of the GSB around 450 nm for both nanoclusters were fitted and compared (Fig. 5C).

For $Pt_1Ag_{24}$, the kinetic traces can be well fitted by a single exponential decay with a time constant of 1.9 μs, whereas for $Pt_1Ag_{28}$, two exponential decays (300 ns, 2.9 μs) were required to obtain the best fitting quality. Further femtosecond transient absorption measurements were performed, and the ultrafast relaxation dynamics for both clusters indeed exhibited similar behavior, which contain an ultrafast and a long lived decay (Fig. S10†). The fluorescence decays measured using time-correlated single-photon counting (TCSPC) exhibit lifetimes similar to that obtained from ns-TA measurements (*cf.* Fig. 5C and D), which suggests that the decay components in $Pt_1Ag_{24}$ and $Pt_1Ag_{28}$ clusters are all radiative.

The long-lived decay in silver nanoclusters has been ascribed to ligand to metal charge transfer (LMCT) but the origin of which is not fully understood.[21b,22b,35–37] As the crystal structures of $Pt_1Ag_{24}$ and $Pt_1Ag_{28}$ are different, it would be helpful to compare the excited state behavior between the homosilver $Ag_{25}$ and $Ag_{29}$ nanoclusters with their Pt doped counterparts, which have similar structures.[21a,22a,38] Table S3† lists the excited state lifetimes of $Ag_{25}$ and $Ag_{29}$ from the literature together with those of $Pt_1Ag_{24}$ and $Pt_1Ag_{28}$ obtained in this study. Both $Ag_{25}$ and $Ag_{29}$ have relatively low fluorescence (QYs < 1%).[21a,22a] From $Ag_{25}$ to $Pt_1Ag_{24}$, the lifetime slightly increases from 1.1 μs (ref. 21b) to 1.9 μs, whereas from $Ag_{29}$ to $Pt_1Ag_{28}$ the lifetime increases from 300 ns (ref. 22b) to dual lifetimes (300 ns and 3.3 μs). The more drastic change in lifetime from $Ag_{29}$ to $Pt_1Ag_{28}$ suggests that the electronic structure is more strongly modified in the case of $Pt_1Ag_{28}$, which may enhance the LMCT and lead to a higher fluorescence quantum yield. Moreover, prominent coherent oscillations were observed in the femtosecond kinetic traces of $Pt_1Ag_{24}$, whereas no such phenomenon was observed for $Pt_1Ag_{28}$ (Fig. S11†). The stronger phonon emission observed in $Pt_1Ag_{24}$ suggests that more excited-state energy is dissipated into the environment through heat, which also explains its weaker luminescence than that of $Pt_1Ag_{28}$.

### Thermal stability

In addition to the PL properties, we further investigated the stability of $Pt_1Ag_{24}$ and its etching product, $Pt_1Ag_{28}$ (Fig. 6). The stability of these NCs was tested at 50 °C in air (NCs dissolved in $CHCl_3$). As to $Pt_1Ag_{28}$, the UV-vis spectra were essentially unchanged over time (12 hours tested), which indicates its high stability, whereas the UV-vis spectra of $Pt_1Ag_{24}$ significantly decrease in intensity after two hours and completely disappear in approximately six hours. The higher thermal stability of $Pt_1Ag_{28}$ than that of $Pt_1Ag_{24}$ was ascribed to the more robust tetrahedral structure than the icosahedral one of $Pt_1Ag_{24}$.

The stability of $Pt_1Ag_{24}$ and $Pt_1Ag_{28}$ was also characterized *via* TGA measurements. As depicted in Fig. S12b and d,† the maximum weight loss temperature of $Pt_1Ag_{24}$ was 240 °C (*i.e.* the derivative curve), which was much lower than that of $Pt_1Ag_{28}$ (310 °C). It should be noted that the 220 °C peak in $Pt_1Ag_{28}$

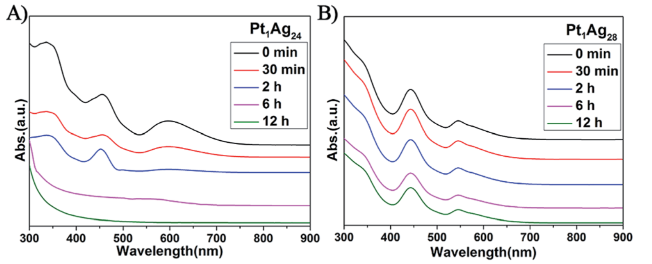


Fig. 6 UV/Vis spectra confirming the thermal stability at 50 °C of the (A) $Pt_1Ag_{24}$ and (B) $Pt_1Ag_{28}$ NCs over time.

corresponds to the loss of $PPh_3$ ligands, which are easier to lose compared to the thiolate ligands. Bakr and co-workers reported that the lack of $PPh_3$ ligands did not alter the overall configuration of $Ag_{29}$ and $Au_1Au_{28}$.[22] Thus, we suspect that the configuration of $Pt_1Ag_{28}$ was maintained at this stage. These results indicate higher stability of $Pt_1Ag_{28}$ compared to that of $Pt_1Ag_{24}$.

# 4 Conclusion

In summary, we devised an etching method for the conversion of $Pt_1Ag_{24}(SPhMe_2)_{18}$ to $Pt_1Ag_{28}(S\text{-}Adm)_{18}(PPh_3)_4$ in the presence of Adm-SH and $PPh_3$. The central Pt atom is retained in the conversion process; however, the $Pt_1Ag_{12}$ kernel was converted from an icosahedron to FCC arrangement, which is observed for the first time in the $M_{13}$ kernel of alloy NCs. Multiple tetrahedral motifs were identified in the alloy NC, such as the $Ag_4S_6P_1$ surface motif, the integrated motif shell $Ag_{16}S_{18}P_4$, and the overall metal framework. The PL QY is significantly increased from only 0.1% for $Pt_1Ag_{24}$ to 4.9% for $Pt_1Ag_{28}$ (about a 50-fold enhancement). The ultrafast dynamics results reveal that the enhanced luminescence of $Pt_1Ag_{28}$ was due to the suppressed phonon emission and other non-radiative pathways in the tetrahedral structure. In addition, the thermal stability of $Pt_1Ag_{28}$ was drastically enhanced compared to that of its precursor, $Pt_1Ag_{24}$. It is hoped that this study will help stimulate the future discovery of new alloy NCs with tailored functionalities for wide applications in sensing and energy fields.

# Acknowledgements

M. Z. acknowledges the financial support provided by the NSFC (21372006, U1532141 & 21631001), the Ministry of Education, the Education Department of Anhui Province and 211 Project of Anhui University. R. J. acknowledges the financial support obtained from the U.S. Air Force Office of Scientific Research (AFOSR) under the AFOSR Award No. FA9550-15-1-9999 (FA9550-15-1-0154) and the Camille Dreyfus Teacher-Scholar Awards Program.

# Notes and references

1 R. Jin, C. Zeng, M. Zhou and Y. Chen, *Chem. Rev.*, 2016, **116**, 10346.
2 K. L. Dimuthu, M. Weerawardene and C. M. Aikens, *J. Am. Chem. Soc.*, 2016, **138**, 11202.
3 C. P. Joshi, M. S. Bootharaju and O. M. Bakr, *J. Phys. Chem. Lett.*, 2015, **6**, 3023.
4 S. Yanazoe, K. Koyasu and T. Tsukuda, *Acc. Chem. Res.*, 2014, **47**, 816.
5 N. Goswami, Q. Yao, Z. Luo, J. Li, T. Chen and J. Xie, *J. Phys. Chem. Lett.*, 2016, **7**, 962.
6 A. Mathew and T. Pradeep, *Part. Part. Syst. Charact.*, 2014, **31**, 1017.
7 W. Kurashige, Y. Niihori, S. Sharma and Y. Negishi, *J. Phys. Chem. Lett.*, 2014, **5**, 4134.
8 W. W. Xu, Y. Gao and X. C. Zeng, *Sci. Adv.*, 2015, **1**, e1400211.
9 S. Yamazoe, S. Takano, W. Kurashige, T. Yokoyama, K. Nitta, Y. Negishi and T. Tsukuda, *Nat. Commun.*, 2016, **7**, 10414.
10 S. Tian, Y.-Z. Li, M.-B. Li, J. Yuan, J. Yang, Z. Wu and R. Jin, *Nat. Commun.*, 2015, **6**, 8667.
11 S. Wang, S. Jin, S. Yang, S. Chen, Y. Song, J. Zhang and M. Zhu, *Sci. Adv.*, 2015, **1**, e1500441.
12 H. –C. Weissker, H. B. Escobar, V. D. Thanthirige, K. Kwak, D. Lee, G. Ramakrishna, R. L. Whetten and X. Lopez-Lozano, *Nat. Commun.*, 2014, **5**, 3785.
13 O. Lopez-Acevedo, K. A. Kacprzak, J. Akola and H. Häkkinen, *Nat. Chem.*, 2010, **2**, 329.
14 M. Azubel, J. Koivisto, S. Malola, D. Bushnell, G. L. Hura, A. L. Koh, H. Tsunoyama, T. Tsukuda, M. Pettersson, H. Häkkinen and R. D. Kornberg, *Science*, 2014, **345**, 909.
15 G. Li, H. Abroshan, Y. Chen, R. Jin and H. J. Kim, *J. Am. Chem. Soc.*, 2015, **137**, 14295.
16 K. Kwak, Q. Tang, M. Kim, D. –E. Jiang and D. Lee, *J. Am. Chem. Soc.*, 2015, **137**, 10833.
17 X.-D. Zhang, Z. Luo, J. Chen, X. Shen, S. Song, Y. Sun, S. Fan, F. Fan, D. T. Leong and J. Xie, *Adv. Mater.*, 2014, **26**, 4565.
18 Y. Zhu, H. Qian, M. Zhu and R. Jin, *Adv. Mater.*, 2010, **22**, 1915.
19 (*a*) C. Zeng, Y. Chen, C. Liu, K. Nobusada, N. L. Rosi and R. Jin, *Sci. Adv.*, 2015, **1**, e1500425; (*b*) C. Zeng, Y. Chen, K. Iida, K. Nobusada, K. Kirschbaum, K. J. Lambright and R. Jin, *J. Am. Chem. Soc.*, 2016, **138**, 3950; (*c*) T. Higaki, C. Liu, C. Zeng, R. Jin, Y. Chen, N. L. Rosi and R. Jin, *Angew. Chem., Int. Ed.*, 2016, **55**, 6694.
20 (*a*) H. Yang, Y. Wang, H. Huang, L. Gell, L. Lehtovaara, S. Malola, H. Häkkinen and N. Zheng, *Nat. Commun.*, 2013, **4**, 2422; (*b*) J. Yan, H. Su, H. Yang, S. Malola, S. Lin, H. Häkkinen and N. Zheng, *J. Am. Chem. Soc.*, 2015, **137**, 11880.
21 (*a*) C. P. Joshi, M. S. Bootharaju, M. J. Alhilaly and O. M. Bakr, *J. Am. Chem. Soc.*, 2015, **137**, 11578; (*b*) M. S. Bootharaju, C. P. Joshi, M. R. Parida, O. F. Mohammed and O. M. Bakr, *Angew. Chem., Int. Ed.*, 2016, **55**, 922.
22 (*a*) L. G. AbdulHalim, M. S. Bootharaju, Q. Tang, S. D. Gobbo, R. G. AbdulHalim, M. Eddaoudi, D. –E. Jiang and O. M. Bakr, *J. Am. Chem. Soc.*, 2015, **137**, 11970; (*b*) G. Soldan, M. A. Aljuhani, M. S. Bootharaju, L. G. AbdulHalim, M. R. Parida, A. –H. Emwas, O. F. Mohammed and O. M. Bakr, *Angew. Chem., Int. Ed.*, 2016, **55**, 5749.
23 Z. Lei, X. –Y. Pei, Z. –G. Jiang and Q. –M. Wang, *Angew. Chem., Int. Ed.*, 2014, **53**, 12771.

24 Y. Wang, X. –K. Wan, L. Ren, H. Su, G. Li, S. Malola, S. Lin, Z. Tang, H. Häkkinen, B. K. Teo, Q. –M. Wang and N. Zheng, *J. Am. Chem. Soc.*, 2016, **138**, 3278.
25 (*a*) S. Wang, X. Meng, A. Das, T. Li, Y. Song, T. Cao, X. Zhu, M. Zhu and R. Jin, *Angew. Chem., Int. Ed.*, 2014, **53**, 2376; (*b*) X. Kang, S. Wang, Y. Song, S. Jin, G. Sun, H. Yu and M. Zhu, *Angew. Chem., Int. Ed.*, 2016, **55**, 3611; (*c*) X. Kang, L. Xiong, S. Wang, H. Yu, S. Jin, Y. Song, T. Chen, L. Zheng, C. Pan, Y. Pei and M. Zhu, *Chem.–Eur. J.*, 2016, **22**, 17145.
26 (*a*) C. Kumara, C. M. Aikens and A. Dass, *J. Phys. Chem. Lett.*, 2014, **5**, 461; (*b*) C. Kumara, K. J. Gagnon and A. Dass, *J. Phys. Chem. Lett.*, 2015, **6**, 1223.
27 S. Xie, H. Tsunoyama, W. Kurashige, Y. Negishi and T. Tsukuda, *ACS Catal.*, 2012, **2**, 1519.
28 H. Qian, D. –E. Jiang, G. Li, C. Gayathri, A. Das, R. R. Gil and R. Jin, *J. Am. Chem. Soc.*, 2012, **134**, 16159.
29 T. Udayabhaskararao, Y. Sun, N. Goswami, S. K. Pal, K. Balasubramanian and T. Pradeep, *Angew. Chem., Int. Ed.*, 2012, **51**, 2155.
30 (*a*) C. Yao, J. Chen, M. –B. Li, L. Liu, J. Yang and Z. Wu, *Nano Lett.*, 2015, **15**, 1281; (*b*) L. Liao, S. Zhou, Y. Dai, L. Liu, C. Yao, C. Fu, J. Yang and Z. Wu, *J. Am. Chem. Soc.*, 2015, **137**, 9511.
31 M. A. Tofanelli, T. W. Ni, B. D. Phillips and C. J. Ackerson, *Inorg. Chem.*, 2016, **55**, 999.
32 S. Wang, Y. Song, S. Jin, X. Liu, J. Zhang, Y. Pei, X. Meng, M. Chen, P. Li and M. Zhu, *J. Am. Chem. Soc.*, 2015, **137**, 4018.
33 (*a*) C. Zeng, T. Li, A. Das, N. L. Rosi and R. Jin, *J. Am. Chem. Soc.*, 2013, **135**, 10011; (*b*) C. Zeng, H. Qian, T. Li, G. Li, N. L. Rosi, B. Yoon, R. N. Barnett, R. L. Whetten, U. Landman and R. Jin, *Angew. Chem., Int. Ed.*, 2012, **51**, 13114.
34 (*a*) C. Zeng, H. Qian, T. Li, G. Li, N. L. Rosi, B. Yoon, R. N. Barnett, R. L. Whetten, U. Landman and R. Jin, *Angew. Chem., Int. Ed.*, 2012, **51**, 13114; (*b*) J. Li, X. Li, H.-J. Zhai and L.-S. Wang, *Science*, 2003, **299**, 864; (*c*) W. Huang, S. Bulusu, R. Pal, X. C. Zeng and L.-S. Wang, *ACS Nano*, 2009, **3**, 1225.
35 M. Pelton, Y. Tang, O. M. Bakr and F. Stellacci, *J. Am. Chem. Soc.*, 2012, **134**, 11856.
36 M. Zhou, J. Zhong, S. Wang, Q. Guo, M. Zhu, Y. Pei and A. Xia, *J. Phys. Chem. C*, 2015, **119**, 18790.
37 M. Zhou, H. Qian, M. Y. Sfeir, K. Nobusada and R. Jin, *Nanoscale*, 2016, **8**, 7163.
38 S. M. Aly, L. G. AbdulHalim, T. M. D. Besong, G. Soldan, O. M. Bakr and O. F. Mohammed, *Nanoscale*, 2016, **8**, 5412.